

# Dynamically Actuated Liquid-Infused Poroelastic Film with Precise Control over Droplet Dynamics

Inkyu Oh, Christoph Keplinger, Jiaxi Cui, Jiehao Chen, George M. Whitesides, Joanna Aizenberg, and Yuhang Hu\*

Traditional dynamic adaptive materials rely on an atomic/molecular mechanism of phase transition to induce macroscopic switch of properties, but only a small number of these materials and a limited responsive repertoire are available. Here, liquid as the adaptive component is utilized to realize responsive functions. Paired with a porous matrix that can be put in motion by an actuated dielectric elastomer film, the uncontrolled global flow of liquid is broken down to well-defined reconfigurable localized flow within the pores and conforms to the network deformation. A detailed theoretical and experimental study of such a dynamically actuated liquid-infused poroelastic film is discussed. This system demonstrates its ability to generate tunable surface wettability that can precisely control droplet dynamics from complete pinning, to fast sliding, and even more complex motions such as droplet oscillation, jetting, and mixing. This system also allows for repeated and seamless switch among these different droplet manipulations. These are desired properties in many applications such as reflective display, lab-on-a-chip, optical device, dynamic measurements, energy harvesting, and others.

has led to unprecedented capabilities such as autonomous actuation and sensing,<sup>[1,2]</sup> controlled release,<sup>[3]</sup> self-healing,<sup>[4]</sup> self-regulation,<sup>[5]</sup> self-reporting,<sup>[6]</sup> self-cleaning,<sup>[7]</sup> antifouling,<sup>[8]</sup> tunable optical properties,<sup>[9,10]</sup> and others. Such conventional materials with adaptive responses often rely on compounds with specific chemical properties that undergo various phase transitions at the atomic/molecular scale to enable macroscopic dynamic behavior in the form of piezoelectric, pyroelectric, electrochromic, shape memory effects, and so on.<sup>[11–15]</sup> The limited availability of the solids that undergo such atomic/molecular transitions is a major constraint. Our quest for new dynamic adaptive materials has to go beyond the search for specific materials formulations and to adopt a bioinspired strategy of designing a hybrid materials system comprising a combination of multiple components

responding to various stimuli with coupled energy transduction mechanisms across the system.<sup>[16–18]</sup> Moreover, different from traditional engineering materials that rely on carving, extruding, rolling, weaving, and molding of solids, Nature's tool box goes far beyond just a solid. Instead, Nature seamlessly and ubiquitously mixes and matches different solids and

## 1. Introduction

Traditional man-made materials are static in form and function. In contrast, nature creates materials that are dynamic and responsive. Only relatively recently synthetic materials chemists began to shift their attention to stimuli-responsive compounds, which

I. Oh, J. Chen, Prof. Y. Hu  
Department of Mechanical Science and Engineering  
University of Illinois at Urbana-Champaign  
Urbana, IL 61801, USA

Prof. C. Keplinger  
Department of Mechanical Engineering  
University of Colorado  
Boulder, CO 80309, USA

Prof. C. Keplinger  
Materials Science and Engineering Program  
University of Colorado  
Boulder, CO 80309, USA

Dr. J. Cui  
INM – Leibniz Institute for New Materials  
Campus D2 2, 66123 Saarbrücken, Germany

Prof. G. M. Whitesides, Prof. J. Aizenberg  
Department of Chemistry and Chemical Biology  
Harvard University  
Cambridge, MA 02138, USA

Prof. G. M. Whitesides, Prof. J. Aizenberg  
Wyss Institute for Biologically Inspired Engineering  
Harvard University  
Cambridge, MA 02138, USA

Prof. G. M. Whitesides, Prof. J. Aizenberg  
Kavli Institute for Bionano Science and Technology  
Harvard University  
Cambridge, MA 02138, USA

Prof. J. Aizenberg  
John A. Paulson School of Engineering and Applied Sciences  
Harvard University  
Cambridge, MA 02138, USA

Prof. Y. Hu  
The George W. Woodruff School of Mechanical Engineering  
Georgia Institute of Technology  
Atlanta, GA 30332, USA  
E-mail: yuhang.hu@me.gatech.edu

DOI: 10.1002/adfm.201802632

liquids to create exquisite properties and functions. Looking at natural examples such as cells, tissues, and organs shows that they are packed with macromolecular networks and interstitial fluid. Actuated by the underneath muscles, the network continuously contracts and expands driving the liquid to flow. As a result, nutrients are exchanged, wastes are expelled, bacteria are blocked, and temperature is regulated.<sup>[19]</sup>

Taking hints from Nature, we propose a new platform for designing and fabricating dynamic adaptive materials: through a multilayer structure, which integrates an artificial muscle and a responsive skin that is composed of a polymeric network and an interstitial liquid. This hybrid system provides a combinational potential to mix and match various inputs and outputs and enables a versatile strategy to expand the current dynamic responsive repertoire. Based on this platform, we fabricate a new dynamic surface that demonstrates precise control over droplet dynamics from free sliding, completely pinning, repetitive stick–slip switching, to extremely fast sliding, droplet oscillation, jetting, and mixing.

## 2. Results and Discussion

### 2.1. Device Design, Fabrication, and Mechanical Analysis

Among a number of materials that have been explored to build artificial muscles, dielectric elastomer (DE) – an elastomeric film sandwiched between two flexible electrodes – provides the outstanding properties close to the true muscle-like actuation, combining high energy densities and efficiencies, large strains, and high actuation frequencies.<sup>[20]</sup> When a voltage is applied across the elastomeric “muscle” film, it contracts in the thickness direction and expands in-plane due to electrostatic attraction between the oppositely charged conducting layers (Figure 1a and Figure S1, Supporting Information). When alternating voltage is applied, the elastomer expands and contracts periodically with respect to the voltage frequencies. To add an adaptive “skin” to the muscle, we introduce a “poroelastic” film that consists of a porous polymeric matrix and an infusing liquid.<sup>[21]</sup> The liquid with its ability to flow and reconfigure is a

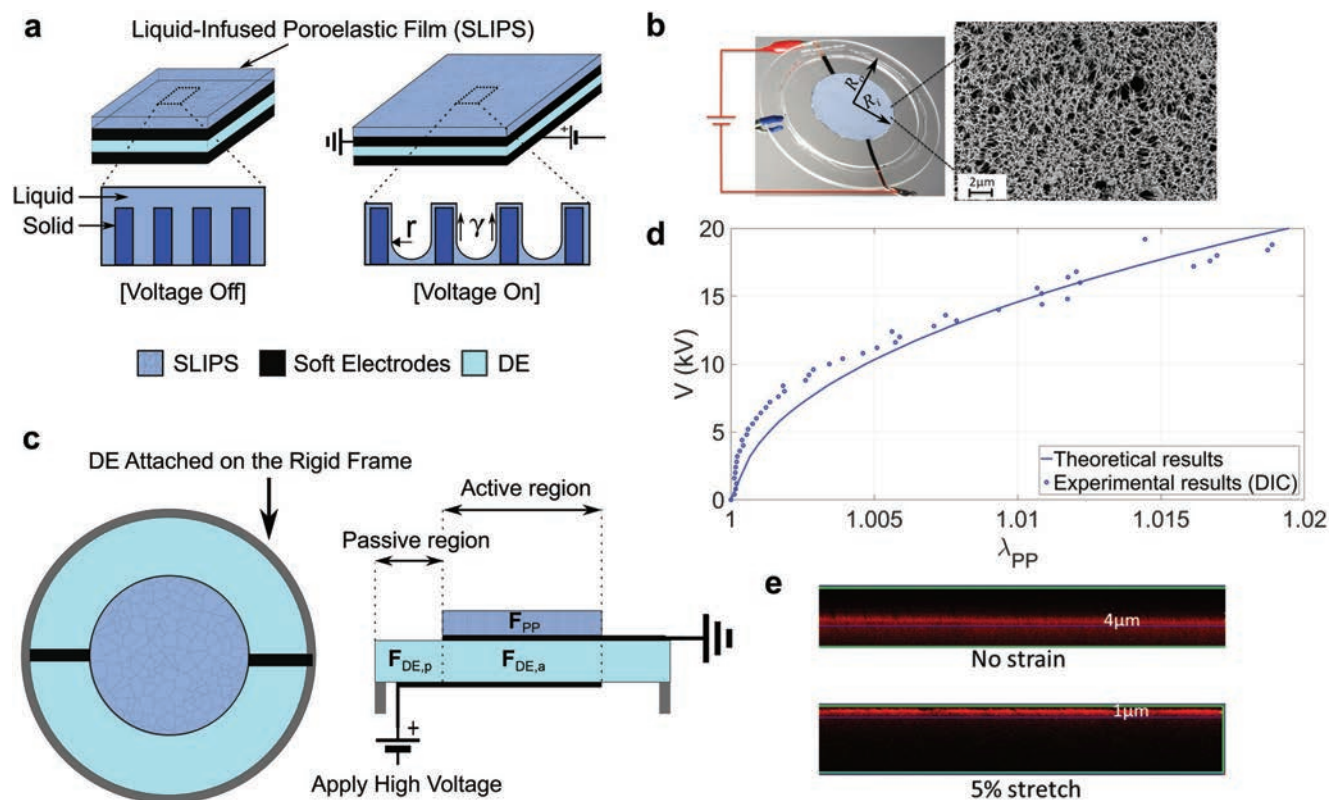


**Figure 1.** Design of the “muscle”-actuated poroelastic “skin”. a) Schematic showing the design and central dynamic reconfiguration mechanism of the system. The device is composed of four layers: a poroelastic film is bonded to an elastomeric film through a conductive and flexible bonding layer, and the opposite side of the elastomer is attached to another layer of a flexible electrode. When a DC voltage is applied, the elastomer contracts in thickness direction and expands in-plane driving the poroelastic film attached on top to deform. The porous matrix of the poroelastic film is illustrated as consisting of uniform pores of radius  $r$ . Initially, a thin layer of excess liquid overcoats the porous film and forms a flat surface. Under tension, the liquid caves into the expanded pores and develops a rough surface. b) A photograph of the constructed device and an SEM image of the porous microstructures of PP film. A white PP film of radius  $R_i$  is attached to a prestretched layer of transparent VHB film that is fixed on a transparent rigid acrylic ring of radius  $R_o$ . The two electrodes on top and bottom of the VHB film are connected with thin strips of copper tapes, which are then connected to the external voltage sources. c) Schematic showing three different regions and their corresponding deformation gradient fields  $F$ . The top and side views of the device at this state are illustrated. d) The stretching ratio of the poroelastic film ( $\lambda_{pp}$ ) is plotted against the amplitude of the external DC voltage ( $V$ ) for both theoretical results (solid line) and experimental measurements (dots). e) Confocal images showing the overcoating film thickness of 4 μm at 0% strain and 1 μm at 5% uniaxial strain.

natural dynamic component for adaptive functions. Paired with a porous matrix that has good chemical affinity to it, the liquid can be stably locked in place. As a result, a continuous overcoating liquid film is formed on the surface. Compared with conventional superhydrophobic surfaces,<sup>[22]</sup> such an atomically flat and mobile liquid interface has demonstrated its superior properties as a repellent surface in many realms, such as self-repair, omniphobicity, and stability under high temperature and pressure.<sup>[21,23]</sup> Recently we have also demonstrated the ability to render the surface properties of liquid-infused materials dynamic and finely tune them or switch them on and off by using either a responsive liquid, such as ferrofluid,<sup>[24]</sup> or a responsive matrix, such as stretchable elastic polymer.<sup>[25]</sup> Further exploration of multifunctional mechanisms that allows for switching of different surface properties in a dynamic fashion is important. Here, we demonstrate a completely new set of dynamic capabilities of the liquid-infused poroelastic film. By synchronizing the flow of the infused liquid with the deformation and actuation of the porous solid skeleton put in motion by the DE muscle, we construct a dynamic surface that can control droplet dynamics from complete pinning, free sliding to fast sliding, and more complex motions such as oscillation, jetting, and mixing. These are desired properties in many applications such as reflective display,<sup>[26]</sup> lab-on-a-chip,<sup>[27–29]</sup> optical device,<sup>[30]</sup> dynamic measurements,<sup>[31]</sup> energy harvesting,<sup>[32]</sup> and others.

The material system is constructed by bonding a poroelastic film to a DE through a layer of conductive glue that serves as both the bonding between the two films and one of the electrodes for DE actuator. The opposite side of the elastomer is attached with another layer of a flexible electrode (Figure 1a and Figure S2, Supporting Information). When voltage is applied across the thickness of the DE, the elastomer deforms and drives the poroelastic film on top to change its shape and size. As a result, the liquid from the overcoating layer is drawn into (or out of) the expanding (or contracting) pores, altering surface topography (Figure 1a). It gives rise to a dynamically adaptive surface that changes between flat and rough in response to mechanical stimuli controlled by voltage signals.

To construct such a material, several important parameters need to be considered. For the poroelastic film, a sufficiently small size of pores and good chemical affinity between the infused liquid and the porous matrix have to be ensured, so the liquid can be stably locked in the pores by capillary and van der Waals forces against gravity. The Poisson's ratio of the porous film has to be smaller than 0.5, for the overall volume of the pore space in the film to change in response to mechanical load. The flow rate of the interstitial liquid through the pores has to be fast enough to catch up with the actuation speed of the solid matrix. Here, we chose polypropylene (PP) porous film, which has the average pore size of 450 nm and Poisson's ratio of 0.41, and infused it with silicone oil that can wick into the PP matrix and form a stable overcoating liquid layer on the outer surface of the film. For the DE, we used a commercial film of very high bond (VHB) 4910 (3M) tape. Three layers of the 1 mm thick VHB elastomer were stacked together, biaxially stretched three times ( $\lambda_{\text{pre}} = 3$ ) and fixed onto a rigid acrylic ring with an open area of radius  $R_0 = 75$  mm (Figure 1b and Figure S2, Supporting Information). The PP film of radius  $R_i = 23.5$  mm was attached to the top surface of the prestretched VHB film

through a layer of conductive glue, serving also as the top electrode of the DE actuator. At the same location where the PP film is attached but on the opposite side of the VHB elastomer, the other electrode of the DE actuator – a layer of carbon grease of the same area as the PP film – was applied. The porous PP film was then filled with silicone oil at the coverage of  $9.8 \mu\text{L cm}^{-2}$ . More details about the device fabrication can be found in the Supporting Information.

When a DC voltage is applied across the thickness of the elastomer, the DE film expands laterally and pulls the attached PP film to deform. To get a better control and rationally design the system's performance, we build a constitutive model for the two-layer system to analytically predict the deformation of the system in response to applied DC voltage. The system can be distinguished into two regions: the active region where the electrodes are attached and the poroelastic film are attached ( $0 < r < R_i$ ), and the passive region where no electrodes are attached ( $R_i < r < R_0$ ; Figure 1c). When a voltage is applied, the active area of the elastomer together with the PP film on top expands in the in-plane direction and the passive area of the elastomer contracts. We assume perfect bonding between the DE film and PP film in the active region. The PP film is modeled as Neo-Hookean material. Its strain energy density can be expressed as

$$W_{\text{PP}}(\mathbf{F}_{\text{PP}}) = \frac{\mu_{\text{PP}}}{2} \left[ \det \mathbf{F}_{\text{PP}}^{\frac{2}{3}} \mathbf{F}_{\text{PP}} : \mathbf{F}_{\text{PP}} - 3 \right] + \frac{K_{\text{PP}}}{2} [\det \mathbf{F}_{\text{PP}} - 1]^2 \quad (1)$$

where  $\mu_{\text{PP}}$  is the shear modulus,  $K_{\text{PP}}$  the bulk modulus, and  $\mathbf{F}_{\text{PP}}$  the deformation gradient of the PP film. The measured shear and bulk moduli of PP film are  $\mu_{\text{PP}} = 12.91$  MPa and  $K_{\text{PP}} = 67.44$  MPa, which were measured from tensile test (see the Supporting Information).

To model the constitutive behavior of DE in the active region, we adapt the framework developed by Suo and co-workers.<sup>[33–35]</sup> The free energy function of the DE film can be expressed as

$$W_{\text{DE,a}}(\mathbf{F}_{\text{DE,a}}, \tilde{\mathbf{E}}) = \frac{\mu_{\text{DE}}}{2} [\mathbf{F}_{\text{DE,a}} : \mathbf{F}_{\text{DE,a}} - 3] - \frac{\epsilon}{2} (\mathbf{F}_{\text{DE,a}}^{-\text{T}} \tilde{\mathbf{E}}) \cdot (\mathbf{F}_{\text{DE,a}}^{-\text{T}} \tilde{\mathbf{E}}) \quad (2)$$

where  $\tilde{\mathbf{E}}$  is the nominal electric vector field,  $\epsilon$  the dielectric permittivity,  $\mu_{\text{DE}}$  the shear modulus, and  $\mathbf{F}_{\text{DE,a}}$  the deformation gradient of the DE in the active region. The passive region of the DE is modeled as incompressible Neo-Hookean material. Its free energy function is

$$W_{\text{DE,p}}(\mathbf{F}_{\text{DE,p}}) = \frac{\mu_{\text{DE}}}{2} [\mathbf{F}_{\text{DE,p}} : \mathbf{F}_{\text{DE,p}} - 3] \quad (3)$$

where the shear modulus of DE is  $\mu_{\text{DE}}$ , and  $\mathbf{F}_{\text{DE,p}}$  is the deformation gradient of the DE in the passive region. In the numerical calculation, the material properties of DE are adopted from a previous study as  $\mu_{\text{DE}} = 68$  kPa, and  $\epsilon = 3.98 \times 10^{-11}$  (F/m).<sup>[35]</sup> While the active region of the DE together with the attached PP film undergoes homogeneous deformation, the passive region undergoes inhomogeneous deformation. The nominal stress field  $\mathbf{s}$  in the passive region has to satisfy

$$\text{div } \mathbf{s} = \tilde{\mathbf{0}}. \quad (4)$$

The nominal stress tensor can be obtained from the free energy function as  $s = \partial W / \partial F$ . Given boundary conditions, the deformation of the system in response to the actuation voltage can be solved numerically. More details of the calculation can be found in the Supporting Information. As shown in Figure 1d, the calculated results of the stretching ratio of the PP film  $\lambda_{pp}$  as a function of the applied DC voltage  $V$  on the DE compare well with the experimentally measured values obtained from the digital image correlation technique.<sup>[36]</sup> All the values of the parameters used in the simulation are obtained directly from experimental measurements, and no fitting parameters are used.

The actuation strain on the PP porous film can be tuned by controlling the prestretching ratio of the DE  $\lambda_{pre}$ , the moduli of the DE film  $\mu_{DE}$  and PP film  $\mu_{pp}$ , the thicknesses of the DE film  $H_{DE}$  and PP film  $H_{pp}$ , and the sizes of the active region  $R_i$  and passive region  $R_o$  (Figure S3, Supporting Information). More details of the parametric studies are shown in Figure S4 in the Supporting Information, in which the mechanical and electrical breakdown points of the DE actuator are also discussed. When voltage is applied on the DE film, the porous PP film on top is stretched homogeneously with the equibiaxial stress ( $\sigma_x = \sigma_y = \sigma$ ). The pressure of the liquid inside the porous matrix decreases instantaneously, with the pressure drop  $\Delta P = -\sigma/3$ , which causes the liquid interface to cave inward until an equilibrium state is reached, and then the pressure difference is balanced by capillary forces at the interface, that is  $-\Delta P = 2\gamma/r_m$ , with  $\gamma$  being the interfacial energy between the infused liquid and the outside media and  $r_m$  the radius of the meniscus curvature in the pores (Figure 1a). When the voltage is removed from the DE film, the tensile stress on the PP film is released, and the pressure difference disappears. The liquid moves back and forms a flat interface again. Confocal images of the overcoating liquid layer before and after stretch are shown in Figure 1e. The original roughly  $4 \pm 0.5 \mu\text{m}$  thick liquid layer becomes approximately  $1 \pm 0.5 \mu\text{m}$  when 5% uniaxial strain is developed on the porous film. For a bigger strain, the liquid caves into the pores and no fluorescent signals are

captured. The dynamic actuation of the system is controlled by the voltage applied across the thickness of the DE film, and the response time of the reconfigurable topography is limited by the flow rate of the liquid in the pores. Based on poroelasticity,<sup>[37]</sup> the diffusivity of a liquid in a porous matrix scales as  $D \sim \mu_{pp} r_p^2 / \eta$ , where  $\mu_{pp}$  is the shear modulus of the matrix,  $\eta$  is the dynamic viscosity of the infused liquid, and  $r_p$  is the radius of the pores. With the following numbers measured for the materials used in this study,  $\mu_{pp} = 12.91 \text{ MPa}$ ,  $r_p = 225 \text{ nm}$ ,  $\eta = 0.096 \text{ kg m}^{-1} \text{ s}$ , the diffusivity of the silicone oil in PP film is estimated to be around  $6.8 \times 10^{-6} \text{ m}^2 \text{ s}^{-1}$ . The time it takes for the infused silicone oil to flow through a distance comparable to the thickness of the film ( $\approx 100 \mu\text{m}$ ) is around  $9.4 \times 10^{-4} \text{ s}$ . Therefore, for an actuation frequency that is smaller than 1 kHz, the liquid in the pores will be able to respond without significant delay.

## 2.2. Dynamic Control of Droplet Mobility

The mechanically tunable topography of the poroelastic film provides a way to dynamically control the sliding and pinning of a liquid droplet that is immiscible with the infused liquid in the porous film (Figure 2a). In the relaxed state, the surface of the poroelastic film is smooth, and the droplet on top slides at a low tilting angle  $\alpha_i$ . When the poroelastic film is stretched, it generates an undulating surface that increases the friction between the droplet and the surface,<sup>[25]</sup> and the droplet slides at a higher tilting angle  $\alpha_h$ . This variable wettability is similar to the previously reported superhydrophobic crumpled graphene films on the DE that exhibit tunable roughness and contact angle in response to the different stretching states of the substrate.<sup>[9]</sup> Beyond the control over the contact angle of a static droplet, here we demonstrate the control over dynamic droplet movement. When the poroelastic film is placed at an angle that is larger than  $\alpha_i$  but smaller than  $\alpha_h$ , the originally sliding droplet on the poroelastic film will be pinned when the film is stretched to the extent that results in the droplet to slide at a higher angle  $\alpha_h$ . For precise control, the contact

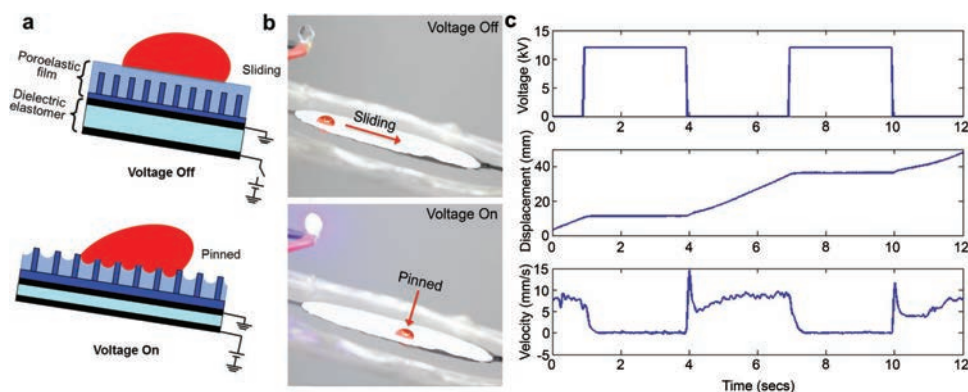


**Figure 2.** Dynamic control of liquid droplet mobility. a) Schematic illustration of the control mechanism: a liquid droplet changes from sliding to pinning as the surface of the poroelastic film changes from flat to rough in response to the mechanical stimuli induced by the voltage signal applied across the underlying DE film. b) Demonstration of the control of the dynamic surface over droplet mobility. A 50  $\mu\text{L}$  water droplet is placed on the silicone-oil-infused PP porous film positioned at a  $7^\circ$  tilting angle, sliding down until a 12 kV voltage is applied across the underlying DE film. The LED is used to indicate the “on” and “off” states of the voltage signal. c) Periodic voltage of a step function form with amplitude of 12 kV and periodicity of 6 s is applied. The applied voltage signal, the recorded displacement of the droplet placed on the upper side of the tilted film, and the velocity of the droplet on the film are plotted as functions of time.

angle hysteresis and sliding angle of water droplets on the silicone-oil-infused PP porous film are measured and shown in Figure S5 in the Supporting Information as a function of strain. For example, the sliding angle of a 50  $\mu\text{L}$  water droplet on the unstretched film is  $5^\circ$ , and becomes  $10^\circ$  when a 15% uniaxial strain is applied to the film. The DE-actuated silicone-oil-infused PP film is placed at a  $7^\circ$  tilting angle. To show the robustness and wide working range of the device, here we demonstrate its function on a relatively big droplet – a 50  $\mu\text{L}$  water droplet (Figure 2b). On the relaxed oil-infused PP film without actuation, the average sliding speed of the droplet – the overall displacement of the droplet over the traveling time – is  $6 \text{ mm s}^{-1}$ . Then, a 12 kV voltage across the thickness of the DE is switched on and off in a square wave form with a periodicity of 6 s. When the voltage is applied, the DE expands in the lateral direction and stretches the oil-infused PP film on top. A light-emitting diode is connected as a signal indicator. When the voltage is on, the light is on, and the water droplet is immediately pinned on the surface. When the voltage is off, the light is off, and the water droplet resumes sliding. Because of the periodic pinning, the average sliding speed of the droplet becomes lower than  $6 \text{ mm s}^{-1}$  (Figure S6, Supporting Information). The sliding displacement of the water droplet is recorded by tracking the front contact line of the droplet from the video and the velocity of the droplet is obtained as a function of time (Figure 2c). The switching control is robust and repeatable as shown in Movie S1 in the Supporting Information.

### 2.3. Dynamic Control of Droplet Moving Speed

When an AC voltage is applied to the DE elastomer, the film is stretched and relaxed periodically. As the actuation frequency increases, due to the inertial effect, the magnitude of the in-plane deformation decreases (Figure S1d, Supporting Information), while the out-of-plane oscillation of the two-layer system becomes significant and peaks when the actuation frequency is close to the transverse resonant frequencies of the membrane system.<sup>[38]</sup> The resonant frequency of the system is related to the geometry, size, and material properties of the system. For the device used in this study, it resonates at 23, 32, 53, 67, 89, 154, and 261 Hz, as shown in Movie S2 in the Supporting Information.

The dynamic interaction between the liquid droplets and the transverse oscillation of the poroelastic film provides a way to modulate the sliding speed of the liquid droplets in a wide range. As an example, a 10  $\mu\text{L}$  water droplet is placed onto the DE-actuated oil-infused PP film that is positioned at  $10^\circ$  tilting angle to demonstrate this capability. The sliding behavior of the water droplet is recorded over a wide range of actuation frequencies in Movie S3 in the Supporting Information. The average sliding speed of the droplet over several periods of actuations is measured for each frequency and plotted in Figure 3a. The original data of the droplet displacement and velocity for the several representative frequencies can be found in Figure S7 in the Supporting Information. On the relaxed oil-infused PP film, when voltage is not applied, the average sliding speed of the droplet is  $0.18 \text{ mm s}^{-1}$ . When a periodic on-and-off voltage of 16 kV is applied, the droplet sticks and slips on the

surface, resulting in a slower overall speed. However, such an expected behavior is only detected until the frequency reaches a certain threshold value ( $\approx 0.2 \text{ Hz}$  shown in Figure 3a), at which moment the droplet is decelerated to about  $0.09 \text{ mm s}^{-1}$ . From that point, the system shows completely unexpected behavior: it then begins to accelerate as the frequency increases and, most surprisingly, the sliding speed of the droplet increases dramatically and reaches  $13.8 \text{ mm s}^{-1}$  at 53 Hz and  $18.6 \text{ mm s}^{-1}$  at 67 Hz – two orders of magnitude faster than on the static oil-infused PP film.

The sliding speed of the droplets on the DE-actuated oil-infused PP film depends on several system parameters including the tilting angle, droplet size, amplitude of actuation voltage, viscosity of the liquid droplet, and the surface tension of the droplet liquid and the infused liquid in the substrate. Systematic experiments are carried out to understand this unique behavior and the results are shown in Figure 3b–g. We also carried out repetitive tests under the same testing condition, which confirms the reproducibility of the experimental results as shown in Figure S8 in the Supporting Information. It can be observed that the average sliding velocity increases at higher tilting angle ( $20^\circ$  compared with  $10^\circ$  from Figure 3b), for bigger water droplets (10  $\mu\text{L}$  compared with 5  $\mu\text{L}$  from Figure 3c), and for higher actuation voltages (16 kV compared with 12 kV from Figure 3d). The droplet sliding velocity is also related to the properties of the droplet. Figure 3e shows that the average velocity of the droplet with higher viscosity is lower. The dynamic viscosity of water/glycerol mixture with 1:1 volume ratio is  $6.86 \times 10^{-3} \text{ N s m}^{-2}$ , which is much higher than the viscosity of pure water ( $8.96 \times 10^{-4} \text{ N s m}^{-2}$ ). Figure 3f shows that the average velocity of the droplet with higher surface tension is higher. Here in experiment, a droplet of water mixed with Alconox detergent, which has a lower surface tension of  $25 \text{ mN m}^{-1}$  than water ( $72 \text{ mN m}^{-1}$ ) was used. For a droplet of lower surface tension, the contact area between the droplet and the substrate is larger and the average velocity of the droplet is slower. For comparison, we also test the average velocity of a water droplet placed on the hydrophobic porous membrane without infused oil. As shown in Figure 3g, the average velocity of the water droplet on the hydrophobic dry porous film is slower than on the oil-infused porous film. The reason is because the presence of the infused oil significantly reduces the friction force between the droplet and the substrate. In conclusion, the higher tilt, droplet volume, applied voltage, and droplet surface tension enhance the sliding velocity, while the higher viscosity of the droplet reduces the sliding velocity (Figure 3b–g). However, for all the different conditions, the critical frequencies corresponding to the peak velocities are not altered, unless the device is changed. Therefore, it is evident that the fast sliding of the droplet is primarily due to the resonant transverse oscillation of the substrate.

The fast sliding of the droplet is a result of a coupled effect of transverse oscillation of the substrate, the capillarity of the droplet liquid, and gravity. First, the experimental results show that the critical frequencies at which the droplet reaches peak sliding speed (Figure 3) coincide with the transverse resonant frequencies of the device (Movie S2, Supporting Information). Second, we look into the droplet morphology on the vibrating substrate. High-speed videos were taken to capture the motion

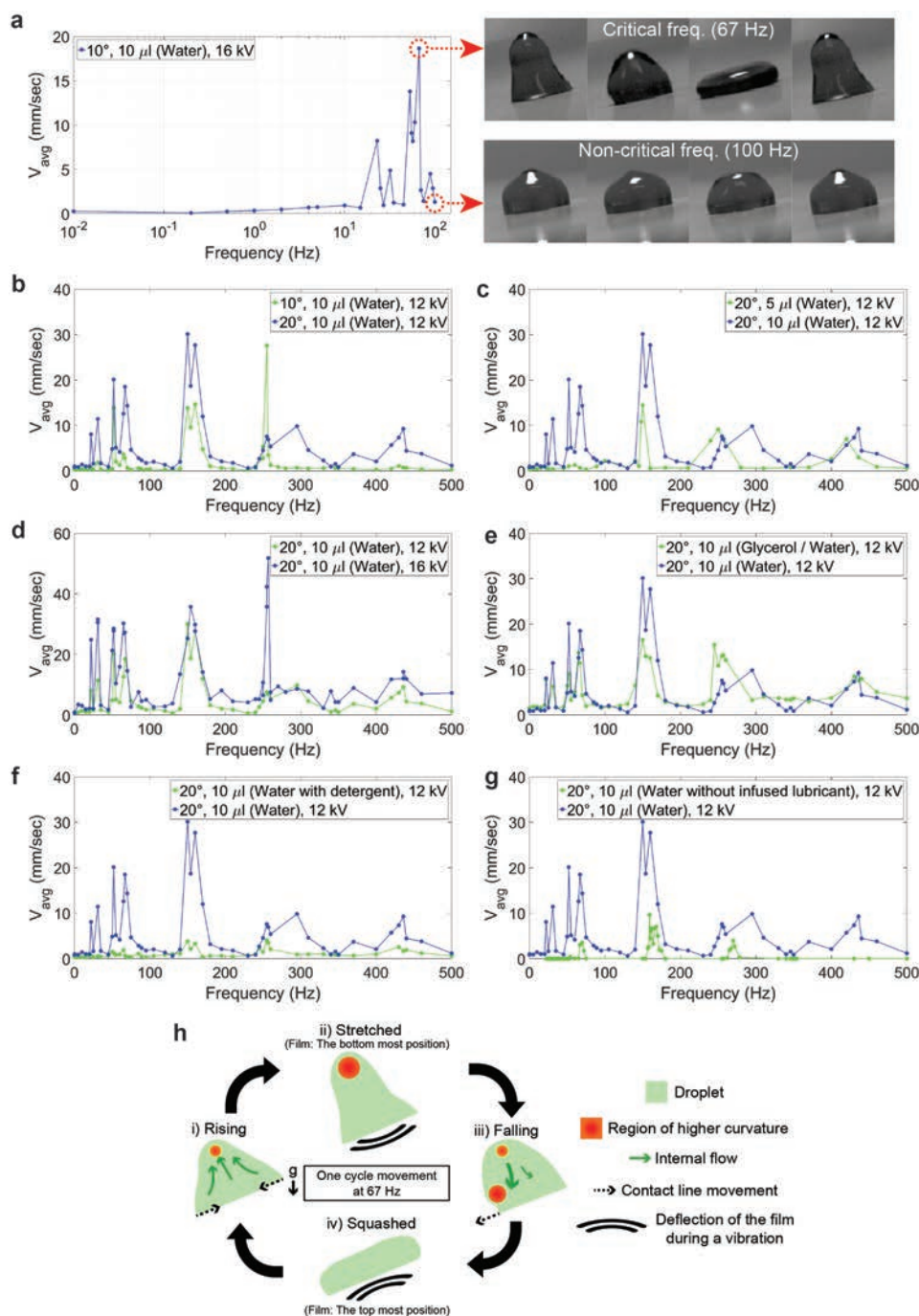


**Figure 3.** Dynamic control of the moving speed of the liquid droplets. a) The average velocity of a 10  $\mu$ l water droplet on the dynamically actuated poroelastic film at 20° tilting angle is plotted as a function of the actuation frequency. The magnitude of the voltage is 16 kV. Peak velocities are observed at critical frequencies of 23, 32, 53, 67, and 89 Hz. Pictures extracted from high-speed videos at 67 Hz (one of critical frequencies corresponding to the peak sliding velocity) and at 100 Hz (the noncritical frequency) show the oscillation morphology of the droplet over a cycle of actuation on a transversely oscillating surface. b–g) The average velocity of water droplets on the dynamically actuated poroelastic film in varying conditions: different b) tilting angle, c) droplet volume, d) amplitude of actuation voltage, e) droplet viscosity, f) droplet surface tension, and g) with and without infused oil in the porous film. h) The schematic of an oscillating and sliding droplet on the oscillating oil-infused poroelastic film at the critical actuation frequency of 67 Hz. The evolution of the droplet shape is categorized into four stages: i) Rising, ii) Stretched; iii) Falling; and iv) Squashed.

of the droplet on the film under different actuation frequencies. Several representative videos are shown in Movie S4 in the Supporting Information, and the snapshots of the morphology

of the mobile droplet (at 67 and 100 Hz) over one period of actuation from this video are shown in Figure 3a. At a lower noncritical frequency, e.g., 5 Hz, the droplet almost remains

its dome shape during the pinning and sliding period. Only at the point of voltage switch does the droplet slightly vibrate and then quickly come back to the stable dome shape. At a higher noncritical frequency, e.g., 100 Hz, the droplet continuously vibrates without clear oscillation pattern as shown in Figure 3a. At the critical frequencies, e.g., 67 Hz corresponding to the peak velocities of droplet sliding, the droplet continuously oscillates up and down in the out-of-plane direction. The transverse vibration of the substrate provides a perturbation to the droplet shape, while capillarity tends to restore the interfacial shape of the droplet like an elastic membrane.<sup>[39]</sup> In Figure 3h, we schematically illustrate the morphology of the droplet over one period of actuation. We separate it into four stages. At the first stage i) Rising, the droplet height rises as it receives the momentum from the vibrating surface. Both the top and bottom contact lines are moving inward, so there is no net movement of the whole droplet at this stage. At the second stage ii) Stretched, the droplet is vertically stretched to the maximum height as the vibrating film reaches to the bottom most position. The top region is highly curved, and the capillarity force tends to pull the liquid droplet downward. At the third stage iii) Falling, as the droplet is pulled down, the front region of the droplet develops higher local curvature as more fluid flows to the front region due to gravity and it makes this local region bulged. This high local curvature pushes the front contact line forward exclusively. As a result, the whole droplet slides down extensively along the surface at this stage. At the last stage iv) Squashed, the droplet achieves the maximum base area and the minimum height as the vibrating film reaches to the top most position. In conclusion, it is the synergistic coupling between the transverse vibrations, the asymmetry of droplet shape due to gravity, and the capillarity that leads to the fast sliding of the droplet – the capillarity converts transverse kinetic energy to the interfacial energy of the droplet and then is

released into the downward-biased momentum with the assist of gravity. More quantitative analysis of the dynamic shape of the droplet and contact line movements on the inclined oscillation device deserves future studies.

#### 2.4. Dynamic Control of Droplet Oscillation, Jetting, and Mixing

The transverse vibration of the DE-actuated poroelastic film also provides a way to realize droplet oscillation, jetting, and quick mixing. As shown in Figure 4a and Movie S5 in the Supporting Information, a 20  $\mu\text{L}$  water droplet continuously oscillates on the horizontally placed device actuated under certain frequencies. The transverse membrane vibration gives perturbation to the droplets, while the capillarity opposes to this perturbation and provides a restoring force. As a result, the droplet exhibits various oscillation modes on the dynamic surfaces (Figure 4a). At 23, 32, 53, and 67 Hz, the droplet oscillates in axisymmetrical modal shapes, while at 89, 154, and 261 Hz, it oscillates in asymmetrical shapes. Such a dramatic oscillation of the droplets can be used to realize rapid mixing. As shown in Figure 4b and Movie S6 in the Supporting Information, the two 20  $\mu\text{L}$  droplets (the yellow one is pure water and the green one is water–glycerol mixture with a volume ratio of 1:1) that are initially placed at a distance apart, become mobile and self-oscillating on the surface when the periodic voltage of 154 Hz is turned on. As soon as the two droplets get in touch, they rapidly mix together. The mixing process takes about 0.2 s. The meeting of the two droplets is more likely to happen at 154 Hz actuation as the droplets are highly mobile even on the horizontal surface. The volume of the droplets tested in this study ranges from a few microliter to tens of microliters. To study the role of infused oil in the substrate on the mixing behavior of droplets,

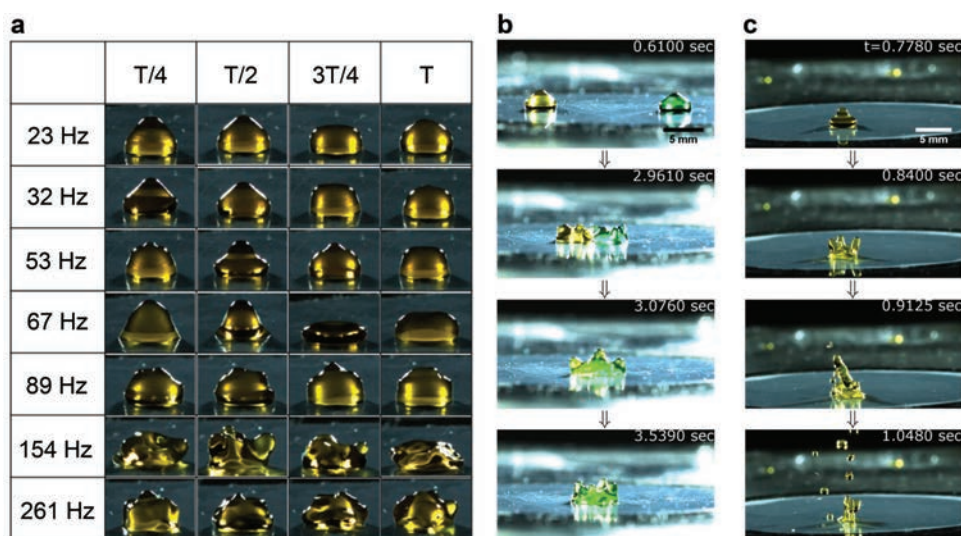


**Figure 4.** Dynamic control of droplet oscillation, jetting and mixing. a) Pictures showing the different oscillation modes of a 20  $\mu\text{L}$  water droplet on a horizontally placed dynamically actuated poroelastic film at frequencies of 23, 32, 53, 67, 89, 154, and 261 Hz with voltage amplitude of 14 kV. Four pictures for each mode of self-oscillation at a time interval of a quarter of the periodicity  $T$ . b) Pictures before, during and after the mixing of two 20  $\mu\text{L}$  droplets (Yellow droplet: pure water. Green droplet: water and glycerol mixture of 1:1 volume ratio) on the dynamic poroelastic film actuated at 147 Hz frequency and 12 kV voltage. c) Pictures in time sequence showing jetting of a 20  $\mu\text{L}$  water droplet placed on the dynamic poroelastic film actuated at 154 Hz frequency and 16 kV voltage.

two identical mixing experiments are performed, one with infusing oil and the other one without infusing oil (Movie S6, Supporting Information). For both cases, we observe the mixing event for 0.1 s using high-speed camera. In the case without infusing oil in the porous substrate, the contact line is pinned even under strong substrate oscillation and thus the internal flow of the liquid in the droplet is constrained. In the case with infusing oil, the droplet contact line is highly mobile and allows for significant internal flow and more effective mixing. On one hand, the transverse vibrations provide a driving force to overcome pinning forces between the droplet and the substrate, and cause the contact line to be mobile.<sup>[40]</sup> On the other hand, the infused oil in the porous substrate reduces the frictional force between the droplet and the substrate. The combination of the two effects leads to fast sliding and effective mixing, faster than previously reported methods.<sup>[41–44]</sup>

As well as oscillation and mixing, the dynamic oscillating poroelastic film can also induce droplet jetting. As is shown in Figure 4c and Movie S7 in the Supporting Information, a 20  $\mu$ L water droplet is placed on the DE-actuated oil-infused PP film. At 154 Hz actuation, one of the resonant frequencies, the droplet vibrates dramatically, resulting in jetting and splitting into small droplets. The oscillation and jetting of the droplet at different actuation frequencies and voltage magnitudes are summarized in Table S1 in the Supporting Information, which can be used as a template for programming and manipulating different droplet dynamics.

### 3. Conclusion

In summary, we present a new approach to creating dynamic adaptive materials that combines actuation and adaptive response components independently through a multilayered architecture. Building upon this platform, we constructed a biomimetic “tissue” by integrating an artificial muscle with a thin layer of a poroelastic skin. This system has demonstrated its ability to access a wide range of finely tuned surface topologies in response to mechanical stimuli that can be automatically controlled by programmed voltage signals. These dynamic reconfigurations will allow us to bring many materials properties, which are sensitive to fine features of the surface topography associated with optics, wettability, adhesion, antifouling, and surface transport characteristics, into the realm of responsive materials. In particular, we have demonstrated the ability to realize comprehensive control over droplet dynamics from complete pinning, free sliding, repetitive stick–slip motions, and extremely fast sliding, to droplet oscillation, jetting, and mixing, which was not seen before in one single material system. Moreover, the system also allows for repeatable and seamless switching among these different manipulations in a programmable and autonomous fashion. The broad range of active droplet behaviors shown in this work result from a coupled effect of droplet dynamics, membrane vibration, fluid dynamics of the infused liquid in small pores, and surface phenomena. The rich physics demonstrated by the new material system creates ample room for future fundamental studies. Toward its practical applications, the material system presented here is light weight, and easy to fabricate, scale up, and integrate into existing structures,

which will make it suitable for many engineering applications. With the development of new DE materials with improved mechanical integrity and low actuation voltage, the newly proposed system can be applied in large structural applications for self-cleaning, controllable condensation, anti-icing, antifouling, and tunable bioadhesion functions.

### Supporting Information

Supporting Information is available from the Wiley Online Library or from the author.

### Acknowledgements

This work was supported by the funding from the Department of Energy, Office of Basic Energy Sciences, Award #: DE-SC0005247. Dr. Y. Hu would also like to acknowledge the funding from National Science Foundation under Grant No. 1554326, and by the Air Force Office of Scientific Research under award number FA9550-17-1-0295. The authors thank Professor R. H. Ewoldt for the help with the high-speed images in his rheology lab.

### Conflict of Interest

The authors declare no conflict of interest.

### Keywords

dynamic droplet control, liquid-infused surfaces, responsive materials

Received: April 17, 2018

Revised: June 11, 2018

Published online: August 1, 2018

- [1] Z. Wang, J. Song, *Science* **2006**, 312, 242.
- [2] D. J. Beebe, J. S. Moore, J. M. Bauer, Q. Yu, R. M. Liu, C. Devadoss, B. Jo, *Nature* **2000**, 404, 588.
- [3] S. Mura, J. Nicolas, P. Couvreur, *Nat. Mater.* **2013**, 12, 991.
- [4] D. A. Davis, A. Hamilton, J. Yang, L. D. Cremer, D. V. Gough, S. L. Potisek, M. T. Ong, P. V. Braun, T. J. Martinez, S. R. White, J. S. Moore, N. R. Sottos, *Nature* **2009**, 459, 68.
- [5] X. He, M. Aizenberg, O. Kuksenok, L. D. Zarzar, A. Shastri, A. C. Balazs, J. Aizenberg, *Nature* **2012**, 487, 214.
- [6] J. Cui, D. Daniel, A. Grinthal, K. Lin, J. Aizenberg, *Nat. Mater.* **2015**, 14, 790.
- [7] T. Sun, G. Wang, L. Feng, B. Liu, Y. Ma, L. Jiang, D. Zhu, *Angew. Chem., Int. Ed.* **2004**, 43, 357.
- [8] P. Shivapooja, Q. Wang, B. Orihuela, D. Rittschof, G. P. Lopez, X. Zhao, *Adv. Mater.* **2013**, 25, 1430.
- [9] J. Zang, S. Ryu, N. Pugno, Q. Wang, Q. Tu, M. Buehler, X. Zhao, *Nat. Mater.* **2013**, 12, 321.
- [10] L. Dong, A. K. Agarwal, D. J. Beebe, H. Jiang, *Nature* **2006**, 442, 551.
- [11] A. Moulson, J. Herbert, *Electroceramics*, Wiley, Chichester **2008**.
- [12] J. M. Jani, M. Leary, A. Subic, M. A. Gibson, *Mater. Des.* **2014**, 56, 1078.
- [13] D. Liu, L. Liu, P. Onck, D. Broer, *Proc. Natl. Acad. Sci. U. S. A.* **2015**, 112, 3880.

- [14] A. P. Dhanarajan, G. P. Misra, R. A. Siegel, *J. Phys. Chem. A* **2002**, *106*, 8835.
- [15] S. N. Semenov, A. S. Y. Wong, R. M. van der Made, S. G. J. Postma, J. Groen, H. W. H. van Roekel, T. F. A. de Greef, W. Huck, *Nat. Chem.* **2015**, *7*, 160.
- [16] J. Capadona, K. Shanmuganathan, D. Tyler, S. Rowan, C. Weder, *Science* **2008**, *319*, 1370.
- [17] R. Yerushalmi, A. Scherz, M. van der Boom, H. Kraatz, *J. Mater. Chem.* **2005**, *15*, 4480.
- [18] M. Stuart, W. Huck, J. Genzer, M. Müller, C. Ober, M. Stamm, G. Sukhorukov, I. Szleifer, V. Tsukruk, M. Urban, F. Winnik, S. Zauscher, I. Luzinov, S. Minko, *Nat. Mater.* **2010**, *9*, 101.
- [19] A. Rawlings, C. Harding, *Dermatol. Ther.* **2004**, *17*, 43.
- [20] P. Brochu, Q. Pei, *Macromol. Rapid Commun.* **2010**, *31*, 10.
- [21] T. Wong, S. Kang, S. Tang, E. Smythe, B. Hatton, A. Grinthal, J. Aizenberg, *Nature* **2011**, *477*, 443.
- [22] D. Quéré, *Rep. Prog. Phys.* **2005**, *68*, 2495.
- [23] S. Wang, K. Liu, X. Yao, L. Jiang, *Chem. Rev.* **2015**, *115*, 8230.
- [24] W. Wang, J. Timonen, A. Carlson, D. Drotlef, C. Zhang, S. Kolle, A. Grinthal, T. Wong, B. Hatton, S. Kang, S. Kennedy, J. Chi, R. Blough, M. Sitti, L. Mahadevan, J. Aizenberg, *Nature* **2018**, *559*, 77.
- [25] X. Yao, Y. Hu, A. Grinthal, T. Wong, L. Mahadevan, J. Aizenberg, *Nat. Mater.* **2013**, *12*, 529.
- [26] R. Hayes, B. Feenstra, *Nature* **2003**, *425*, 383.
- [27] G. Whitesides, *Nature* **2006**, *442*, 368.
- [28] V. Srinivasan, V. Pamula, R. Fair, *Lab Chip* **2004**, *4*, 310.
- [29] S. Cho, H. Moon, C. Kim, *J. Microelectromech. Syst.* **2003**, *12*, 70.
- [30] B. Berge, J. Peseux, *Eur. Phys. J. E* **2000**, *3*, 159.
- [31] J. Timonen, M. Latikka, O. Ikkala, R. Ras, *Nat. Commun.* **2013**, *4*, 2398.
- [32] T. Krupenkin, J. Taylor, *Nat. Commun.* **2011**, *2*, 448.
- [33] X. Zhao, W. Hong, Z. Suo, *Phys. Rev. B* **2007**, *76*, 134113.
- [34] S. Koh, T. Li, J. Zhou, X. Zhao, W. Hong, J. Zhu, Z. Suo, *J. Polym. Sci. B Polym. Phys.* **2011**, *49*, 504.
- [35] T. Li, C. Keplinger, R. Baumgartner, S. Bauer, W. Yang, Z. Suo, *J. Mech. Phys. Solids* **2013**, *61*, 611.
- [36] E. Jones, M. Silberstein, S. White, N. Sottos, *Exp. Mech.* **2014**, *54*, 971.
- [37] M. Biot, *J. Appl. Phys.* **1941**, *12*, 155.
- [38] C. Keplinger, J. Sun, C. Foo, P. Rothemund, G. Whitesides, Z. Suo, *Science* **2013**, *341*, 984.
- [39] P. Gennes, F. Brochard-Wyart, D. Quéré, *Capillarity and Wetting Phenomena*, Springer, New York **2010**, p. 1.
- [40] X. Noblin, A. Buguin, F. Brochard-Wyart, *Eur. Phys. J. E* **2004**, *14*, 395.
- [41] S. Daniel, M. Chaudhury, *Langmuir* **2002**, *18*, 3404.
- [42] A. Buguin, L. Talini, P. Silberzan, *Appl. Phys. A* **2002**, *75*, 207.
- [43] S. Mettu, M. Chaudhury, *Langmuir* **2011**, *27*, 10327.
- [44] J. Longley, E. Dooley, D. Givler, W. Napier, M. Chaudhury, S. Daniel, *Langmuir* **2012**, *28*, 13912.